

Chapter 4

Effect of substitution of non-magnetic impurity Sb on ferromagnetism in dilute Fe doped SnSe

4.1 Introduction

Tin Selenide (SnSe) is a p-type and one of the group IV – VI semiconductors which has currently garnered much attention as an efficient material for thermoelectric applications. Tin Selenide (SnSe) is a material made up of inexpensive, less toxic elements found in abundance on Earth, which greatly increases its value in long-lasting electronic, thermoelectric, photodetector and phase change memory devices [1-4]. Narrow band gap is a property that is ubiquitous in IV – VI group compound semiconductors. The direct and indirect band gap values of bulk SnSe are reported to be 1.3 eV and 0.9 eV respectively [5, 6]. They tend to exist in two phases i.e. α and β , both having orthorhombic crystal structure but different values of lattice parameters as well as space groups (Pnma and Cmcm respectively). However, since the α phase is stable at room temperature, it can only result in normalized performances [7]. On the other hand, β -phase sees a significant rise in the thermoelectric figure of merit (zT) value as it has higher electrical conductivity when compared to the α phase [8]. It also undergoes a transition to cubic structure at 540°C and to tetragonal structure at 860°C [9, 10].

SnSe, when doped with different elements, can have an influence on their different material properties, such as electrical, optical and magnetic properties. Single crystal SnSe doped with Bi was found to give an impressive zT value of around 2.2 at 733 K [11]. Further, an extraordinary zT value of 3.1 at 783 K was observed in Na doped polycrystalline SnSe which has still not been achieved by any other thermoelectric systems [12]. Electronic band structure is an important

deciding factor for how well a material can be utilized for photonics applications. It was found that doping with both a donor impurity Sb and an acceptor impurity In can lead to an increase in the direct and indirect band gap values of single crystal SnSe as compared to pure SnSe crystal [13]. Such variations brought about in the band gap makes it appropriate for solar cell and photocatalytic applications. A similar increase in band gap was also observed in Sb doped SnSe nanocrystals [14]. However, in potassium doped SnSe crystal and Cl doped SnSe nanoparticles, the band gap was found to undergo a contraction thereby leading to an improvement in its electrical conductivity and optoelectronic devices [15, 16]. Band gap is also found to be impacted by the grain size wherein a decrease in its value has been observed as grain size increases [17, 18]. The Raman spectra of Zn doped nanostructured SnSe, in addition to the modes B_{2u} and A_g that correspond to SnSe, there was a presence of an additional peak at 192 cm^{-1} which seems to arise due to a phase transformation in the structure [19]. A red shift of A_g^3 mode and blue shift of B_{3g} and A_g^2 modes were observed as thickness of SnSe nanosheets grown on PDMS increased [20]. A red shift of Raman peaks was also observed in In doped SnSe thin films with its increasing concentration [21]. Electrical resistivity of Na and Ag doped SnSe single crystals are found to show metal-like behaviour and transport property suggests Na to be more effective as a p-type dopant than Ag [22]. Single crystal SnSe exhibits a metallic behaviour in the temperature range 300 K – 525 K. Above 525 K up to 800 K, it is showing semiconducting behaviour that is thermally activated [23].

In the literature review, there was relatively little experimental work pertaining to examining the magnetic properties of doped SnSe. Majority of the work consisted of utilizing the theoretical approach to understand the structural and magnetic properties of samples. From the first principle calculations, it was found that Co, Mn, Fe and Ni doped SnSe monolayer showed magnetism [24]. An antiferromagnetic coupling exists between two Mn atoms whereas a

combination of both antiferromagnetic and ferromagnetic coupling was observed between two-Fe-doped systems. Antiferromagnetic coupling was also observed between Eu^{2+} ions in Eu doped SnSe [25]. In another study, doping with transition metals in SnSe was found to give rise to dilute magnetic semiconducting systems having narrow band gaps and also induce semiconductor-metal and semiconductor-half metal transitions [26]. The multiferroic nature of 2D p-doped SnSe was confirmed from the co-existence of ferroelectricity and ferrimagnetism having a Curie temperature of about 337 K [27].

To fill the gap between theory and experiment, we choose to prepare Fe doped SnSe bulk alloys, where the Fe concentration is kept within the dilute limit of 0.05. How well an increase in carrier concentration can improve its magnetic properties can be examined on substituting group V element Sb into it at varying concentrations. The inherent properties of these samples that have been modified due to doping were probed using different instruments and techniques, the details of which are given briefly in the section that follows.

4.2 Experimental Procedure

SnSe, Fe, and Sb (Alfa Aesar, 99.999% pure) in the desired amounts were measured and filled in quartz tube ampoules in order to make powder samples of $\text{Fe}_{0.05}(\text{SnSe})_{1-x}\text{Sb}_x$ where $x = 0, 0.03$ and 0.05 . Under a pressure of $>10^{-5}$ Torr in a rotary pump, these ampoules were vacuum-sealed. To reach the proper temperature for the powders to melt, the sealed ampoules were frequently heated in an oxy-butane flame. The ampoules were cooled down by placing them in cold water after making sure a thorough mixing of the constituent powders took place. This resulted in the creation of solidified ingots, which were ground and subsequently examined.

Powder X-Ray Diffractometer (XRD) that uses CuK_α radiation having wavelength 1.5406 \AA in the 2θ range of $20^\circ - 70^\circ$ was made use of to analyze the crystal structure properties of the samples. With the help of UV-Visible

spectrometer of Perkin Elmer Lambda 950, optical diffuse reflectance spectra in the wavelength range 500–1500 nm are captured, and the band gap of the samples are determined from these spectra. To understand the kind of vibrational modes present in the samples, Raman studies were performed using a micro-model Raman spectrometer (STR-500). Electrical resistivity studies of samples were examined using Physical Property Measurement System (PPMS) of Quantum design make, which was also used to analyze the magneto-resistance property. The magnetization characteristics of the samples were understood by measuring the data between 10 K and 300 K and in the presence of up to 7 T of magnetic field using a Superconducting Quantum Interface Device (SQUID-VSM) magnetometer fitted with Pulse Tube Cooler.

4.3 Results and Discussion

4.3.1 Structural Studies

$\text{Fe}_{0.05}(\text{SnSe})_{1-x}\text{Sb}_x$ bulk alloys are characterized for their structural properties using X-ray diffractometer (Powder XRD) and the diffraction spectra are shown in Fig. 4.1. The peak values are indexed in the figure, and they were found in accordance with the orthorhombic crystal structure of SnSe having Pnma space group (JCPDF 48-1224). The is presence of no additional impurity peaks which suggests that Fe and Sb atoms are well integrated into the SnSe matrix without bringing about a visible change in its crystal structure. (400) peak has a strong preferential orientation for having a strong intensity as compared to the other peaks. Lattice parameters of the samples are ascertained from the XRD data as well as using plane space formula for orthorhombic structure [28].

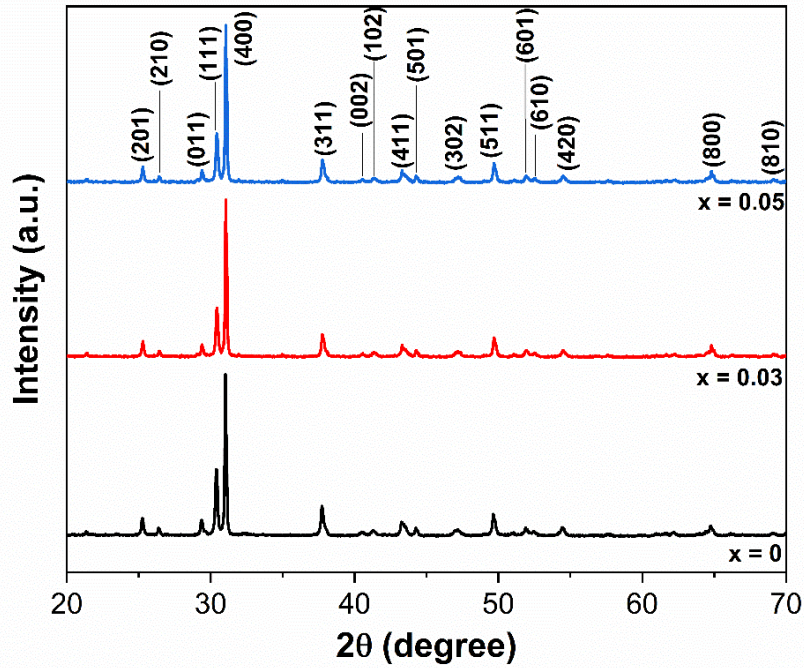


Figure 4.1: XRD diffraction pattern with peak indexing of $Fe_{0.05}(SnSe)_{1-x}Sb_x$ bulk alloys for $x = 0, 0.03$ and 0.05 .

XRD data also helps in determining the values of crystallite size using three approaches i.e. Scherrer's formula, Williamson-Hall (W-H) plot and Size-Stain Plot (SSP). The difference between the three lies in the factor that is responsible for the broadening of the diffraction peaks. Scherrer's formula exclusively considers crystallite size to be the sole factor causing peak broadening whereas W-H plot and SSP consider the defects and strain generated due to doping as the contributing factor [29, 30]. Equations 4.1, 4.2 and 4.3 represent the Scherrer's, W-H and SSP formulae respectively.

$$D = \frac{0.9 \lambda}{\beta \cos \theta} \quad (4.1)$$

$$\beta \cdot \cos \theta = \frac{0.9 \lambda}{D} + 4\varepsilon \cdot \sin \theta \quad (4.2)$$

$$(d_{hkl} \cdot \beta_{hkl} \cdot \cos \theta)^2 = \frac{k\lambda}{D} \cdot (d_{hkl}^2 \cdot \beta_{hkl} \cdot \cos \theta) + \frac{\varepsilon^2}{4} \quad (4.3)$$

Here, D denotes the crystallite size and all other parameters have been previously defined in chapter 3.

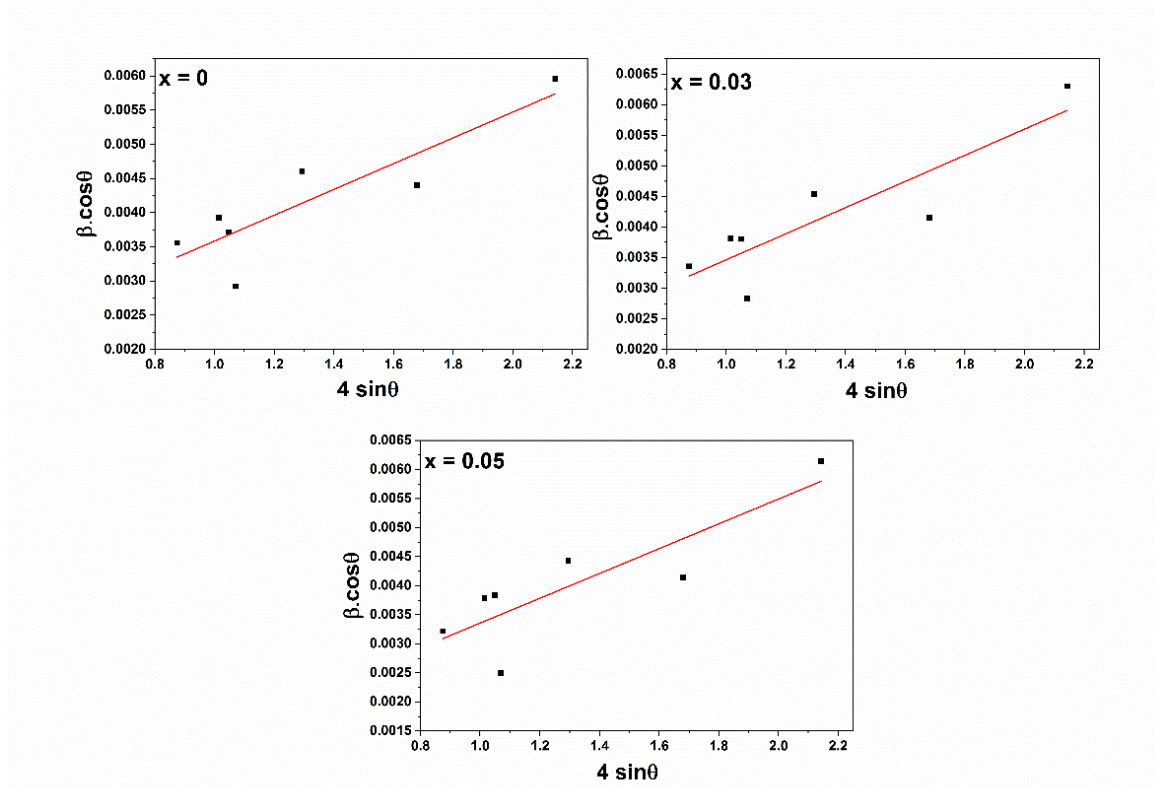


Figure 4.2: Williamson-Hall analysis plot of $Fe_{0.05}(SnSe)_{1-x}Sb_x$ bulk alloys. Red line denotes linear fit to the data.

The plots of $(4 \cdot \sin\theta$ vs $\beta \cdot \cos\theta)$ that correspond to W-H equation are shown in Fig. 4.2. A linear fit is made to the data and from the intercept of this linear fit, crystallite size values are inferred. A positive slope is observed from the plot for all the samples which indicates presence of tensile strain in the system [31]. Similarly, crystallite size from the SSP plots can be evaluated from the slope of $(d_{hkl}^2 \cdot \beta_{hkl} \cdot \cos\theta)$ vs $(d_{hkl} \cdot \beta_{hkl} \cdot \cos\theta)^2$ as shown in Fig. 4.3. Table 4.1 contains a list of the above-mentioned parameter values. The crystallite size values evaluated from the W-H and SSP methods are in good agreement with each other suggesting much more accuracy in the values as compared to that obtained from Scherrer equation. This is because Scherrer's equation considers only size effects on the broadening of peaks as mentioned above.

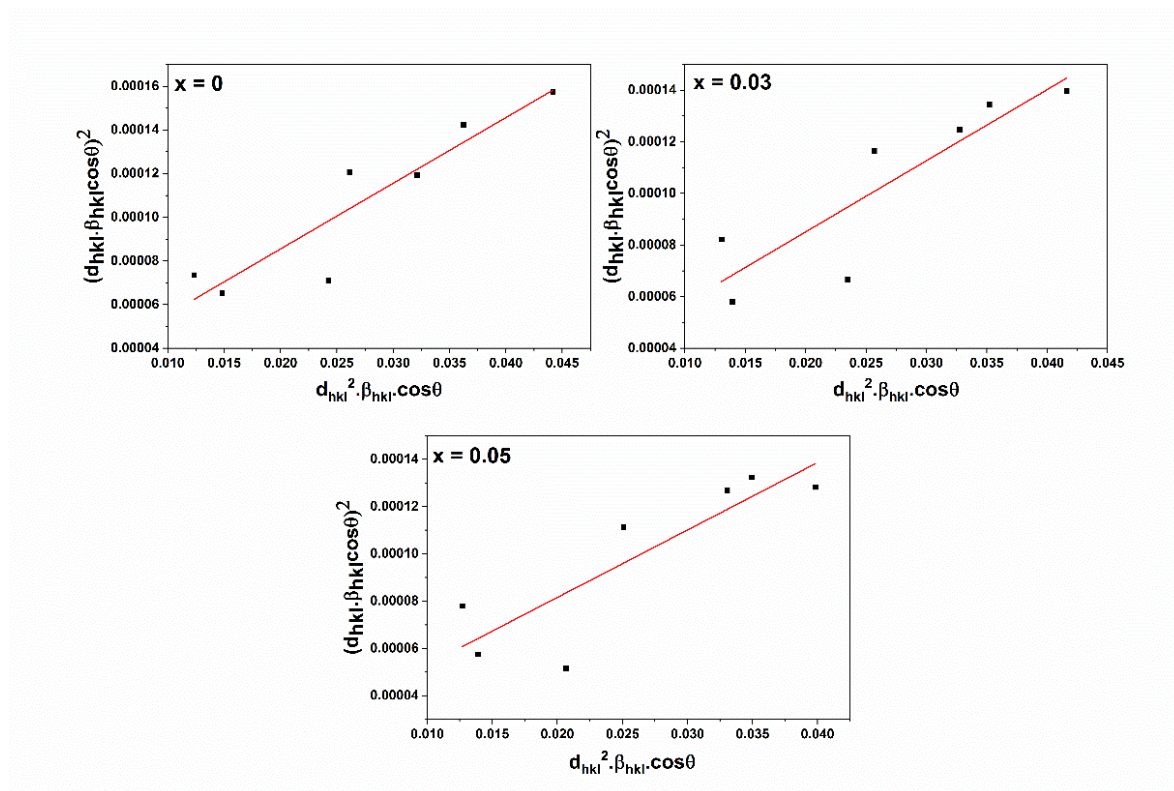


Figure 4.3: Size-Strain plot of $Fe_{0.05}(Te)_{1-x}Sb_x$ bulk alloys. Linear fit to the data is represented by the red line.

Table 4.1: Lattice parameter and Crystallite size values of $Fe_{0.05}(SnSe)_{1-x}Sb_x$ from the XRD data.

Samples	From XRD			Crystallite Size (nm)		
	a (Å)	b (Å)	c (Å)	Scherrer	W-H	SSP
$Fe_{0.05}(SnSe)$	11.526	4.161	4.451	34.826	45.685	46.064
$Fe_{0.05}(SnSe)_{0.97}Sb_{0.03}$	11.508	4.160	4.445	35.557	49.343	50.237
$Fe_{0.05}(SnSe)_{0.95}Sb_{0.05}$	11.501	4.157	4.438	36.962	50.789	51.604

4.3.2 UV-Visible Studies

Since the band gap of bulk SnSe as mentioned above falls in the UV-Visible region, the diffuse reflectance spectra (DRS) of the samples were recorded between the wavelength ranges of 500 – 1500 nm, from which band gap values are determined. Using the DRS spectral data, Kubelka – Munk function

$F(R)$ for each sample is calculated by making use of the Kubelka – Munk (K-M) equation defined as

$$F(R) = \frac{1-R^2}{2R} \quad (4.4)$$

R represents reflectance data. A plot of $(F(R)hv)^{1/n}$ v/s photon energy (hv) for each sample is shown in Fig. 4.4 (a) and (b) where an extrapolation of the linear region of the graph is carried out to touch the X-axis and this corresponds to the optical band gap value. Given that SnSe has both direct and indirect band gap energies, fitting is performed by taking the values of n as $1/2$ and 2 in accord with the direct and indirect allowed transitions respectively. Doping with Fe is seen to cause a narrowing effect on the direct and indirect band gap as the values obtained are 0.97 eV and 0.76 eV respectively. However, with the substitution of Sb, there is only a very moderate increase in the band gap value, to 0.99 eV and 0.81 eV for direct and indirect transitions, respectively. Table 4.2 lists the values of both direct and indirect band gaps for each sample. Thus, no dramatic variation in the band gap values is observed even though the Fermi level seems to be shifting into the conduction band, due to increase in donor impurity, resulting in a trivial change in the band gap value.

Table 4.2: Direct and indirect band gap values of $Fe_{0.05}(SnSe)_{1-x}Sb_x$ samples.

Samples	Direct Band Gap	Indirect Band Gap
	eV	eV
$Fe_{0.05}(SnSe)$	0.97 ± 0.02	0.76 ± 0.02
$Fe_{0.05}(SnSe)_{0.97}Sb_{0.03}$	0.98 ± 0.02	0.80 ± 0.02
$Fe_{0.05}(SnSe)_{0.95}Sb_{0.05}$	0.99 ± 0.02	0.81 ± 0.02

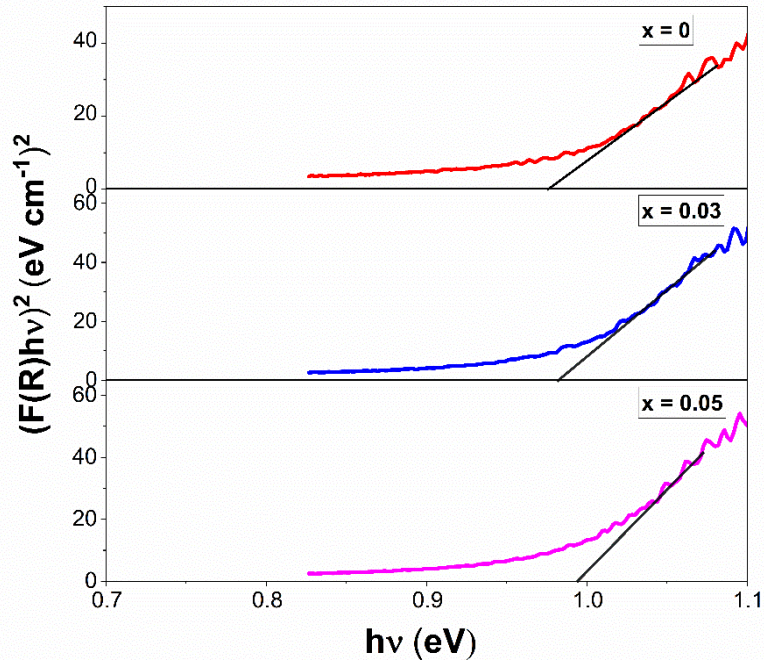


Figure 4.4 (a): Plots of $(F(R)hv)^2$ vs. energy hv to find the direct band gap of $Fe_{0.05}(SnSe)_{1-x}Sb_x$ bulk alloys.

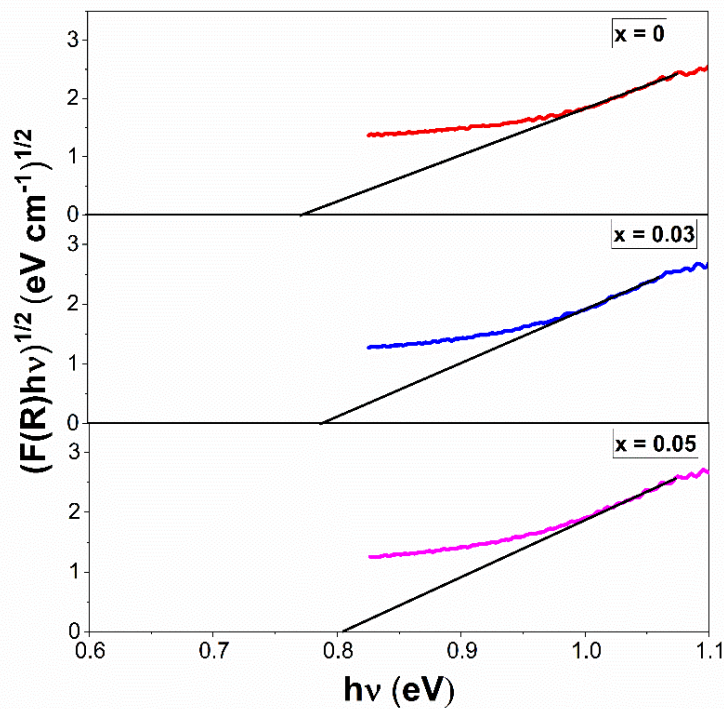


Figure 4.4 (b): Plots of $(F(R)hv)^{1/2}$ vs. energy hv to find the indirect band gap of $Fe_{0.05}(SnSe)_{1-x}Sb_x$ bulk alloys.

4.3.3 Raman Measurements

Based on the symmetry analysis, pure SnSe that possesses an orthorhombic phase was found to have 12 Raman active modes at the center of Brillion zone

namely ($4A_g + 2B_{1g} + 4B_{2g} + 2B_{3g}$) [32]. However, typically only four of these distinctive modes are commonly observed in the Raman spectra i.e. A_g^1 , B_{3g} , A_g^2 and A_g^3 [33]. The signature Raman active peaks of pristine SnSe can be traced at wavenumbers 131 cm^{-1} and 150 cm^{-1} [34]. Fig. 4.5 shows Raman spectra of $\text{Fe}_{0.05}(\text{SnSe})_{1-x}\text{Sb}_x$; $x = 0, 0.03$ and 0.05 samples, carried out at room temperature. A blue shift of the characteristic peaks can be observed on doping with transition element Fe to 152.61 cm^{-1} and 184.23 cm^{-1} . The origin of such a blue shift can be ascribed to the presence of a tensile strain in the system that arises due to doping of Fe. With the substitution of non-magnetic element Sb, the peaks are now found to undergo red shift that corresponds to a shift to lower values of wavenumber. Thus, a compressive strain gets induced in the lattice structure of SnSe due to the presence of additional donor charge carriers through introduction of Sb. Additionally, the intensity of Raman peaks of $x = 0.03$ sample undergoes a rise, whereas the peak intensity of $x = 0.05$ sample exhibits a decrease. Furthermore, the spectra of $x = 0.05$ sample reveal the presence of two extra peaks, one at 164.12 cm^{-1} and the other at 205 cm^{-1} that may be related to the emergence of a Sb-Sb bond and Sb-Se bond respectively. [35, 36]. These new bonds could be responsible for the diminishing of the peak intensity.

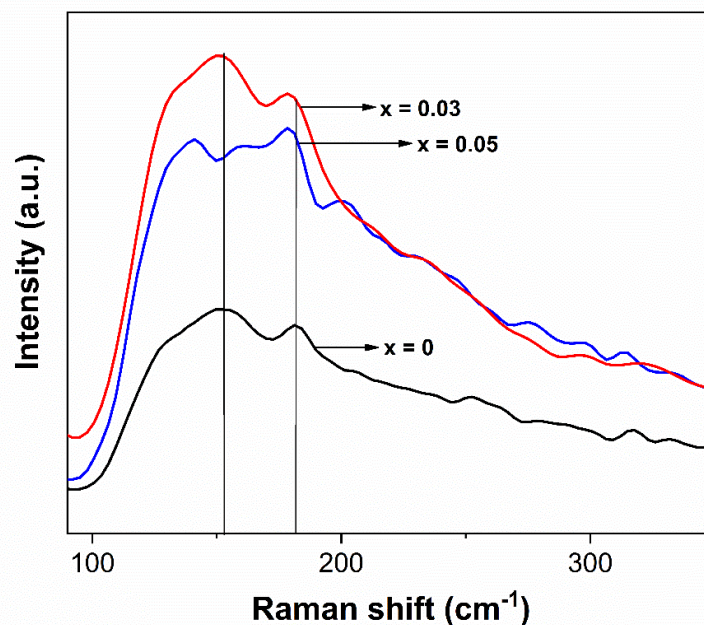


Figure 4.5: Room temperature Raman spectra of $\text{Fe}_{0.05}(\text{SnSe})_{1-x}\text{Sb}_x$ bulk alloys.

4.3.4 DC Resistivity Measurements

To understand the nature of the conduction mechanism projected by the samples, resistivity measurement using the Physical Property Measurement System (PPMS) is an important tool and has been carried out at zero field in the temperature range of 2 K – 300 K. Furthermore, application of an external magnetic field of 5T and 8T will also help to determine the effect an additional magnetic field can have on the resistivity pattern of the samples. The value of resistivity of pure, undoped SnSe lies between (0.1 – 1) Ω -cm. What is significant for the present work is the manipulation of the charge carrier concentration dependence of Sb on the resistivity of Fe doped SnSe for Sb concentrations of 0.03 and 0.05. Figure 4.6(a, b) shows the resistivity curves of $\text{Fe}_{0.05}(\text{SnSe})_{1-x}\text{Sb}_x$; $x = 0.03$ and 0.05 samples.

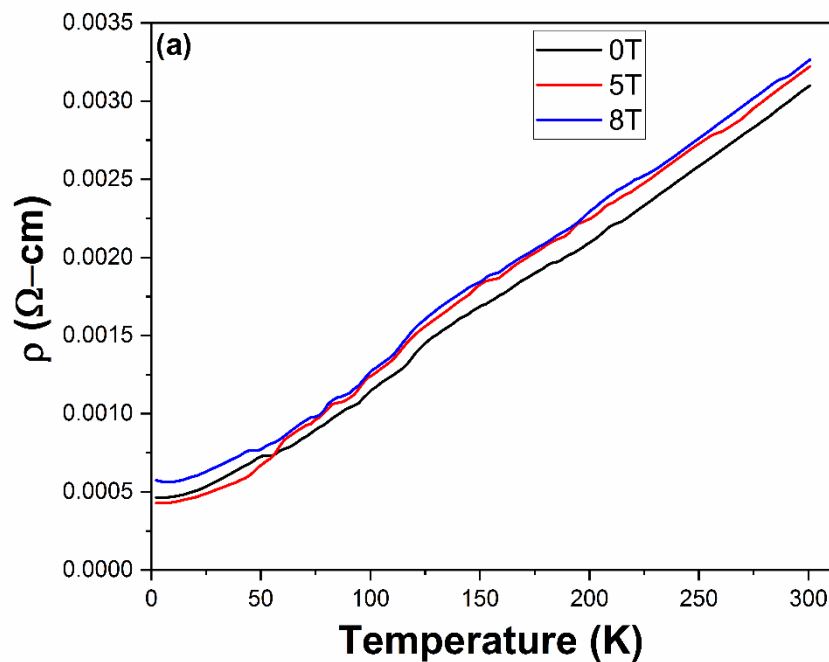


Figure 4.6(a): DC electrical resistivity of $\text{Fe}_{0.05}(\text{SnSe})_{1-x}\text{Sb}_x$ bulk alloy for $x = 0.03$ at 0T, 5T and 8T.

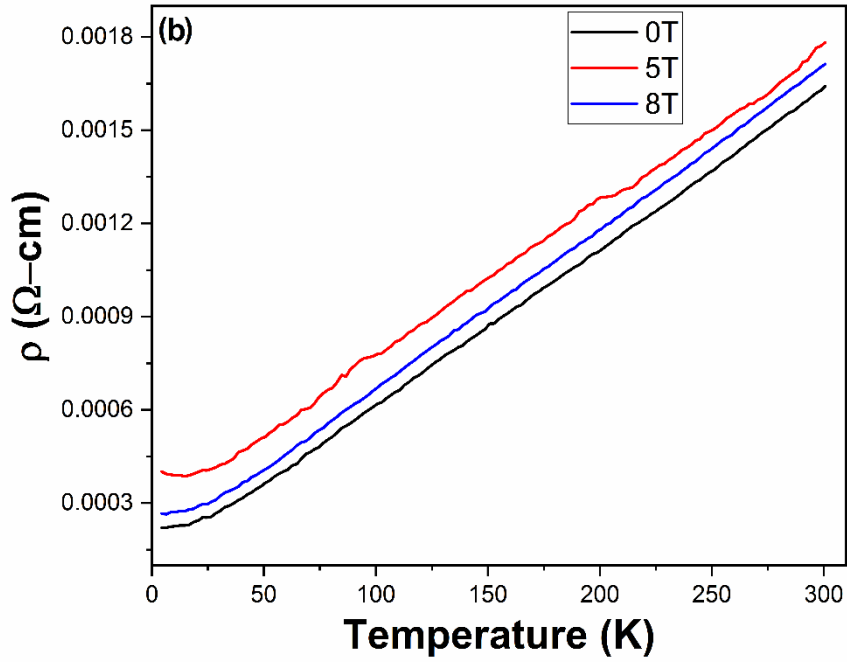


Figure 4.6(b): DC electrical resistivity of $Fe_{0.05}(SnSe)_{1-x}Sb_x$ bulk alloy for $x = 0.05$ at 0T, 5T and 8T.

Typically, SnSe is a non-magnetic, narrow band gap semiconductor [37]. Through doping of Fe that acts as a hole dopant and substitution of Sb wherein donor impurities are added into the system, samples $x = 0.03$ and 0.05 experience an unexpected transition to a purely metallic state as seen in Fig. 4.6(a) and (b).

The transport properties of the applied field dependent resistivity data can be explained by analyzing the experimental data using a qualitative model. This model takes into consideration different interactions and scattering processes like electron-electron scattering, two-magnon scattering, electron-electron interaction, electron-phonon interaction and is represented by the equation defined as follows,

$$\rho = \rho_0 + \rho_e T^{1/2} + \rho_2 T^2 + \rho_{4.5} T^{4.5} + \rho_p T^5 \quad (4.5)$$

where ρ_0 , $\rho_e T^{1/2}$, $\rho_2 T^2$, $\rho_{4.5} T^{4.5}$ and $\rho_p T^5$ stands for residual resistivity, electron-electron interaction, electron-electron scattering, two-magnon scattering and electron-phonon interaction respectively. However, for $x = 0.03$ and 0.05

samples, equation (4.5) does not give an impeccable fitting to the resistivity data at low temperature where the curve seems to have a transition from linear behaviour. This suggests that there could be another additional factor contributing to the transport mechanism. Kondo-like spin dependent scattering mechanism is taken into account to explain the anomaly in the low temperature data. It considers the interaction between the localized spins of the magnetic dopant and the conduction electrons of the host matrix. Thus, equation (5) can now be re-written as,

$$\rho = \rho_0 + \rho_e T^{1/2} - \rho_s \ln T + \rho_p T^5 + \rho_2 T^2 + \rho_{4.5} T^{4.5} \quad (4.6)$$

where $\rho_s \ln T$ denotes the Kondo-like scattering. Figures 4.7(a) and 4.7(b) depict the best fitting to equation (4.6) for $x = 0.03$ and 0.05 samples respectively. The values of parameters for either sample are listed in Table 4.3 and 4.4.

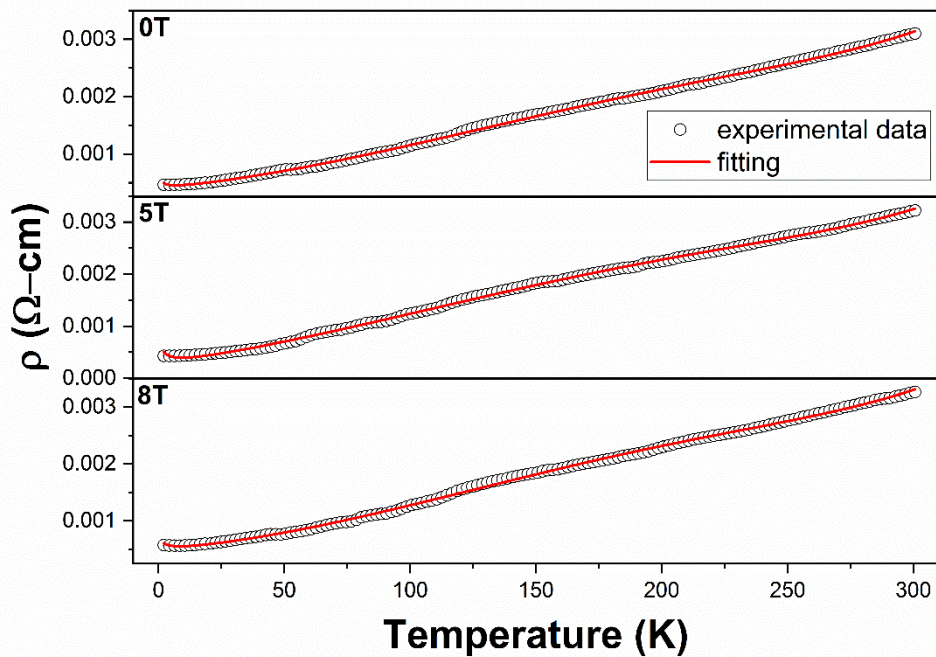


Figure 4.7(a): Fitting of the resistivity data of $Fe_{0.05}(SnSe)_{1-x}Sb_x$ bulk alloy for $x = 0.03$ at $0T$, $5T$ and $8T$ using equation (4.6).

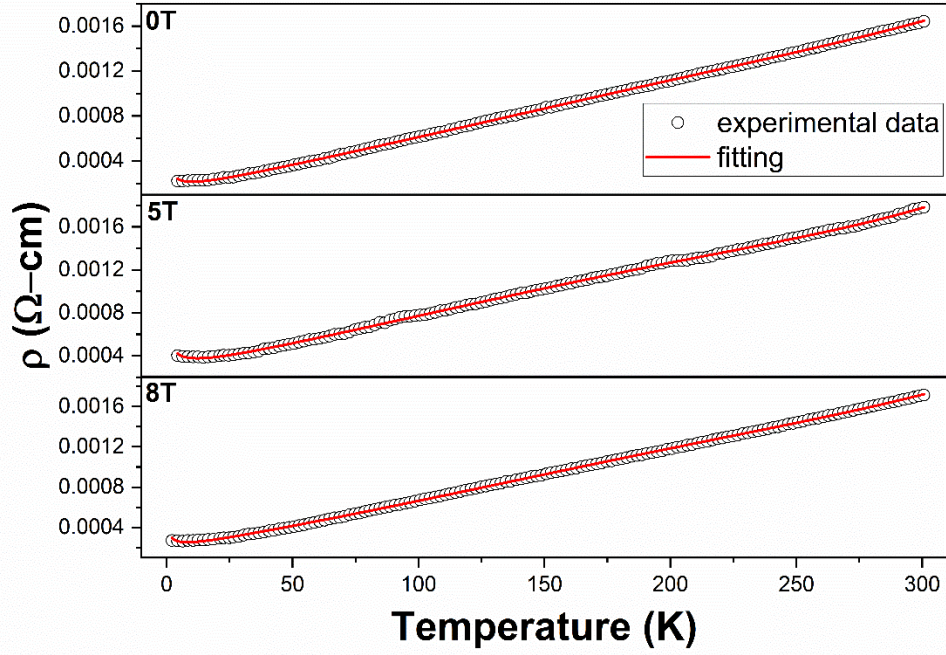


Figure 4.7(b): Fitting of the resistivity data of $Fe_{0.05}(SnSe)_{1-x}Sb_x$ bulk alloy for $x = 0.05$ at 0T, 5T and 8T using equation (4.6).

Table 4.3: Fitting parameters for $Fe_{0.05}(SnSe)_{1-x}Sb_x$; $x = 0.03$ sample.

Applied Magnetic Field	Parameters from eq. (4.6)					
	$\rho_0 \times 10^{-4}$ ($\Omega.cm$)	ρ_e ($\Omega.cm/K^{1/2}$)	$\rho_s \times 10^{-4}$ ($\Omega.cm$)	$\rho_2 \times 10^{-8}$ ($\Omega.cm/K^2$)	$\rho_{4.5} \times 10^{-14}$ ($\Omega.cm/K^{4.5}$)	$\rho_p \times 10^{-15}$ ($\Omega.cm/K^5$)
0T	4.532	8.6589×10^{-5}	1.1803	4.221	-8.529	4.1229
5T	4.629	1.6116×10^{-4}	2.5268	3.724	-8.787	4.2852
8T	5.841	8.9343×10^{-5}	1.3797	4.831	-1.008	4.8355

Table 4.4: Fitting parameters for $Fe_{0.05}(SnSe)_{1-x}Sb_x$; $x = 0.05$ sample.

Applied Magnetic Field	Parameters from eq. (4.6)					
	$\rho_0 \times 10^{-4}$ ($\Omega.cm$)	ρ_e ($\Omega.cm/K^{1/2}$)	$\rho_s \times 10^{-4}$ ($\Omega.cm$)	$\rho_2 \times 10^{-8}$ ($\Omega.cm/K^2$)	$\rho_{4.5} \times 10^{-14}$ ($\Omega.cm/K^{4.5}$)	$\rho_p \times 10^{-16}$ ($\Omega.cm/K^5$)
0T	2.720	9.8849×10^{-5}	1.6104	1.000	-1.359	6.5209
5T	4.793	1.0853×10^{-4}	1.9327	1.09	-2.384	8.1869
8T	5.288	8.3586×10^{-5}	1.2194	1.309	-1.946	9.2573

The value of $\rho_{4.5}$ is negative for both the samples and negative value is an indication of weak contribution of two-magnon scattering in the transport mechanism. From the above tables, it can also be seen that the fitted values of some parameters decrease as the magnetic field increases pointing towards the possibility of suppression of those interactions and scattering processes between the charge carriers within the sample due to magnetic field.

4.3.4 Magnetization Measurements

Magnetization studies of $\text{Fe}_{0.05}(\text{SnSe})_{1-x}\text{Sb}_x$ bulk alloy samples ($x = 0, 0.03$ and 0.05) in the DC mode were performed using a SQUID-VSM magnetometer in the temperature range of 10 K – 300 K spanning over 8T of magnetic field. The magnetic nature of the samples with respect to the temperature can be evaluated from the M-T measurement. There are two ways in which this measurement can be performed, zero field cooled (ZFC) condition and field cooled (FC) condition. In ZFC, samples initially undergo cooling till 10 K in the absence of any field, following which an external magnetic field of 100 Oe is applied accompanied by heating of the samples till the temperature reaches 300 K. Variation occurring in the magnetic moment as a function of temperature is recorded. In case of FC, cooling of samples were carried out by already subjecting them to 100 Oe magnetic field till 10 K followed by the process of heating during which once again magnetic moment v/s temperature data is measured. The plots corresponding to ZFC-FC curves of the samples are illustrated in Fig. 4.8(a-c).

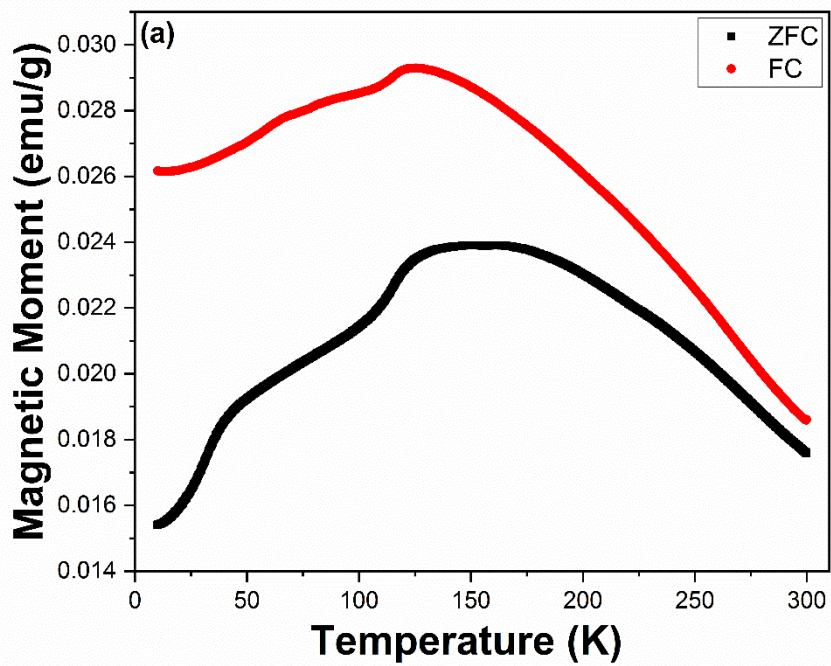


Figure 4.8(a): Magnetization vs Temperature plot under ZFC-FC condition for $x = 0$ sample.

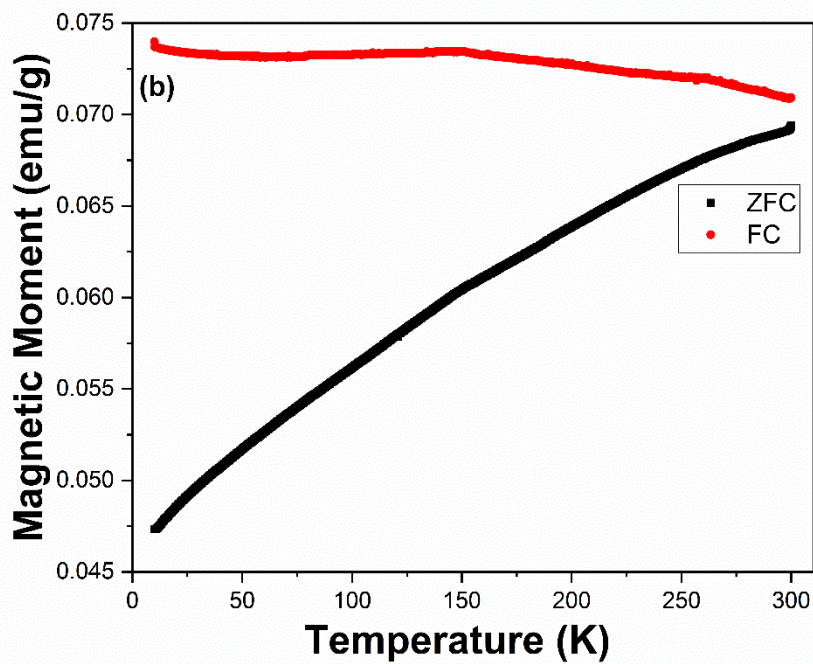


Figure 4.8(b): Magnetization vs Temperature plot under ZFC-FC condition for $x = 0.03$ sample.

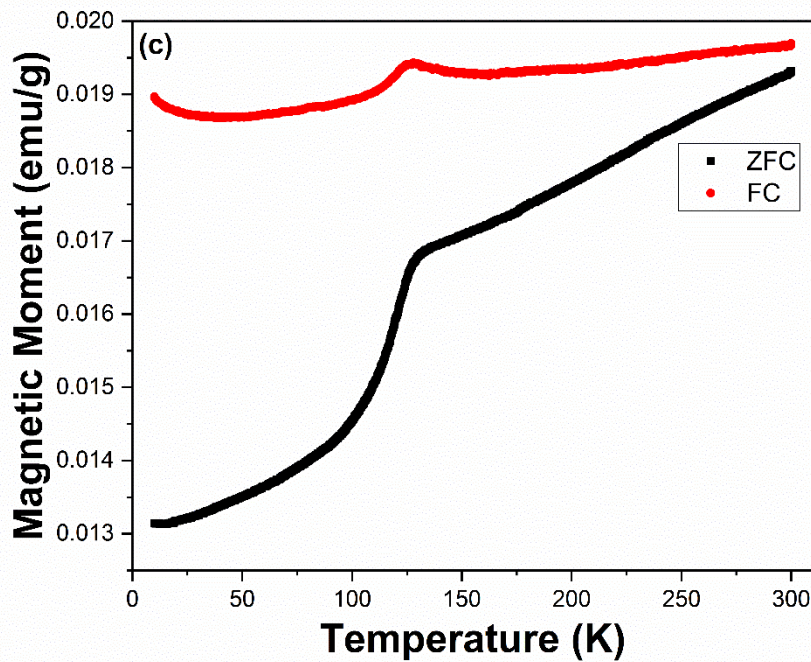


Figure 4.8(c): Magnetization vs Temperature plot under ZFC-FC condition for $x = 0.05$ sample.

The ZFC and FC plots of $x = 0$ sample represent a similar behaviour without any overlapping between the curves. ZFC magnetization curve is found to increase with a decrease in temperature starting from 300 K, reaches a maximum as represented by a broad peak in the curve and then once again decreases with further reduction in temperature. Such a decreasing trend seems to arise due to clusters getting randomly frozen into distinct metastable states [38]. A similar response is also observed for FC magnetization curve. The fall of FC magnetization below the maximum suggests strong anti-ferromagnetic interactions between the magnetic ions [39]. A broad maximum in the curves is observed at about 130 K, which can be referred to as the blocking temperature T_B . There is no overlapping between the curves beyond T_B . As a result, it can also be concluded that at room temperature, the system also contains some superparamagnetic particles that are weakly interacting with each other. The plot of $x = 0.03$ sample on the other hand shows a large separation between the ZFC and FC curves at lower values of temperature. Absence of a maxima in the ZFC

curve suggests that bifurcation goes well beyond the room temperature and that blocking temperature is above 300 K. The continuous decrease of ZFC curve with lowering temperature is reminiscent of weak ferromagnetic moments that are associated with magnetic glassy state. The FC curve is seen to remain fairly the same shape throughout the range of temperature. This seems to arise due to the presence of a strong coupling between ferromagnetic moments of the particles. In $x = 0.05$ sample, both the ZFC and FC curves are found to decrease with decreasing temperature values. However, there is also presence of a hump in the FC and ZFC curve at around 125 K which may relate to magnetic domain pinning effect [40]. As the amount of donor impurities increase, they try to neutralize the holes leading to non-uniform distribution of magnetic ions thereby affecting the domain wall movement. Below the hump, a sudden drop in ZFC curve could indicate a weak existence of spin-glass state in the system due to the spins freezing over.

Hysteresis measurement represented by M-H curve were also performed using SQUID – VSM and the data was recorded at the temperatures 100 K and 300 K in the applied field range of -70 kOe to 70 kOe. The M-H curve of $x = 0$ sample as shown in Fig. 4.9(a) exhibits a clear presence of hysteresis at both 100 K and 300 K having a substantial coercivity values of 2374 Oe and 700 Oe respectively. Such considerable values of coercivity would make the sample appropriate for memory devices that can withhold the information for a longer duration even in the absence of magnetic field. Doping of Fe brings about holes into the system and this induced magnetism is the result of hole mediated indirect exchange interaction between Fe^{2+} ions. On substitution of Sb into the system, a rapid drop in the coercivity value of $x = 0.03$ sample can be seen in Fig. 4.9(b). Sb being non-magnetic in nature, introduces electrons into the system thereby suppressing the hole concentration which was responsible for magnetic interactions. The curve at 100 K has a coercivity value of 99 Oe and that at 300

K has almost negligible hysteresis behaviour which suggests an onset of superparamagnetism beyond room temperature. Such a dramatic decrease in coercivity value seems to arise due to Sb being a donor impurity. Sb tries to compensate for the effects caused by hole dopant Fe in the system thereby suppressing the hysteresis behaviour of the sample. With an increase in the concentration of Sb to $x = 0.05$, the number of electrons in the system also increases. The hysteresis behaviour is seen to enhance yet again resulting in an enhancement in the coercivity value from that of $x = 0.03$ sample. Figure 4.9(c) shows M-H curve of $x = 0.05$ sample and the coercivity values are 253 Oe and 167 Oe for 100 K and 300 K curves respectively. This suggests RKKY-type of exchange interaction between the magnetic ions through donor impurity Sb. Such an increase in coercivity could also be attributed to pinning of the domain walls. This domain wall pinning effect has also been advocated in the M-T curve of $x = 0.05$ sample. The coercivity values of the samples are also presented in Table 4.5.

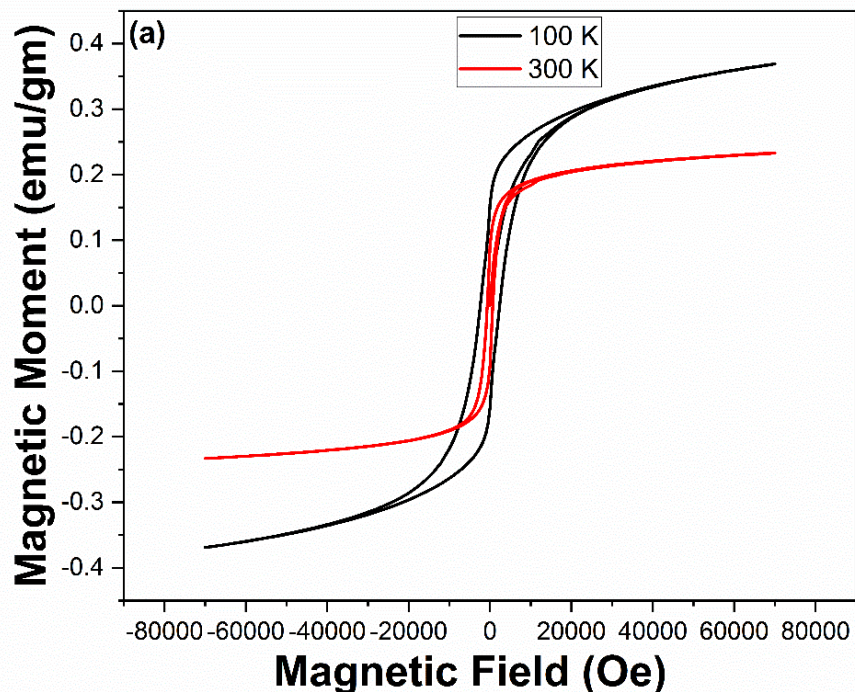


Figure 4.9(a): Hysteresis plot of $Fe_{0.05}(SnSe)_{1-x}Sb_x$ bulk alloy for $x = 0$ at 100 K and 300 K.

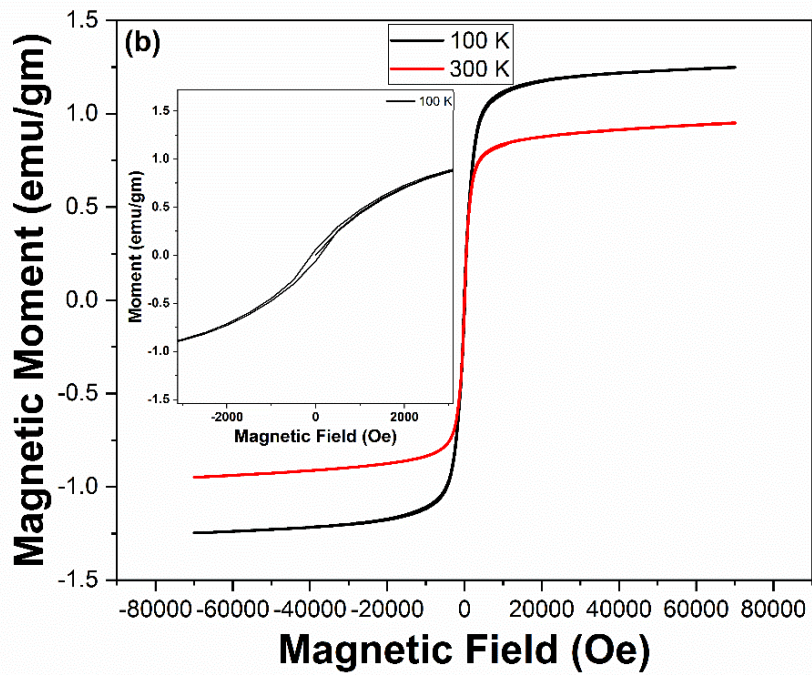


Figure 4.9(b): Hysteresis plot of $Fe_{0.05}(SnSe)_{1-x}Sb_x$ bulk alloy for $x = 0.03$ at 100 K and 300 K. Inset is the magnified view of the plot at 100 K.

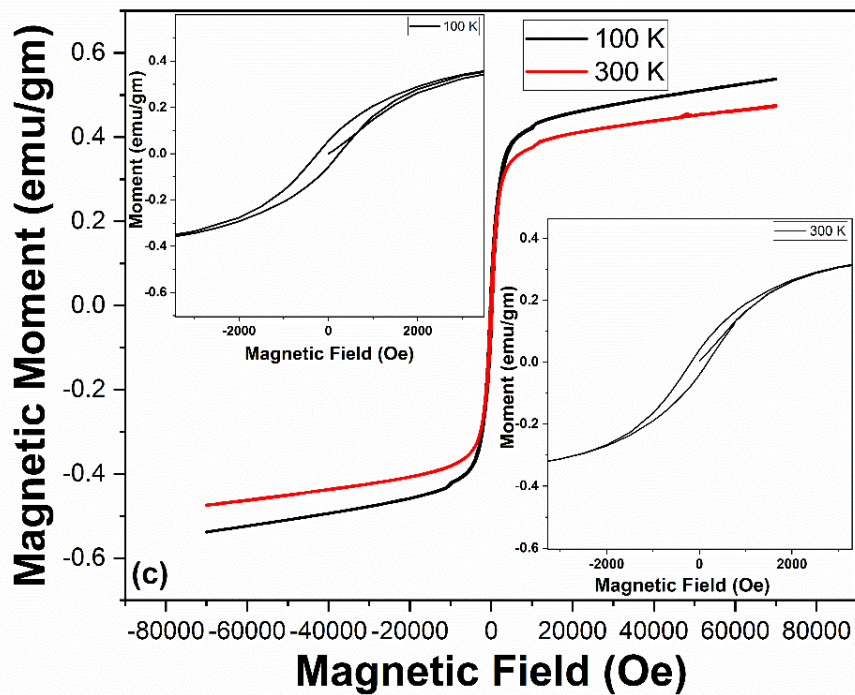


Figure 4.9(c): Hysteresis plot of $Fe_{0.05}(SnSe)_{1-x}Sb_x$ bulk alloy for $x = 0.05$ at 100 K and 300 K. Inset is the magnified view of the plot at 100 K and 300 K.

Table 4.5: Coercivity and Magnetization Saturation values of $Fe_{0.05}(SnSe)_{1-x}Sb_x$ samples.

Samples	Coercivity (H_c) Oe		Magnetization Saturation (M_s) emu/gm	
	100 K	300 K	100 K	300 K
$Fe_{0.05}(SnSe)$	2374	700	-	-
$Fe_{0.05}(SnSe)_{0.97}Sb_{0.03}$	95	-	1.23	N.A.
$Fe_{0.05}(SnSe)_{0.95}Sb_{0.05}$	245	167	-	-

4.3.5 Magnetic Memory Effect Measurement

Using SQUID-VSM, the measurement of magnetic memory effect of $Fe_{0.05}(SnSe)_{1-x}Sb_x$; $x = 0$ and 0.05 samples were carried out from $10\text{ K} - 300\text{ K}$ in the FC condition as per the protocol suggested by Sun et al. [41]. The samples were cooled from 300 K to 10 K in the presence of an external magnetic field of 100 Oe at a cooling rate of 1 K/min . Intermittent stops at 200 , 100 and 50 K for a duration of 1 hour were made and the magnetic field was switched off at each of these temperatures. A step-like magnetization curve can be observed as seen in Fig. 4.10(a, b). On reaching the lowest temperature, the samples were warmed till 300 K in the presence of same magnetic field without any stoppage and once again magnetization was measured. If a step-like curve is observed around each stopping temperature, it indicates that the sample has memorized its spin alignment while cooling and is able to reproduce it while warming the sample. $x = 0$ sample can be seen to retain the memory information at all temperatures.

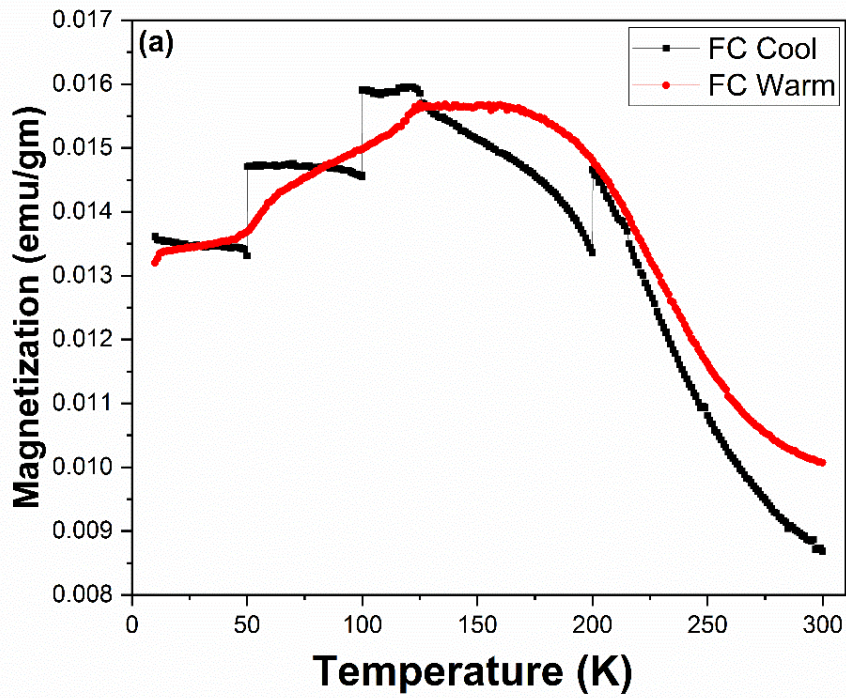


Figure 4.10(a): FC Magnetic memory measurement of $x = 0$ sample at 100 Oe.

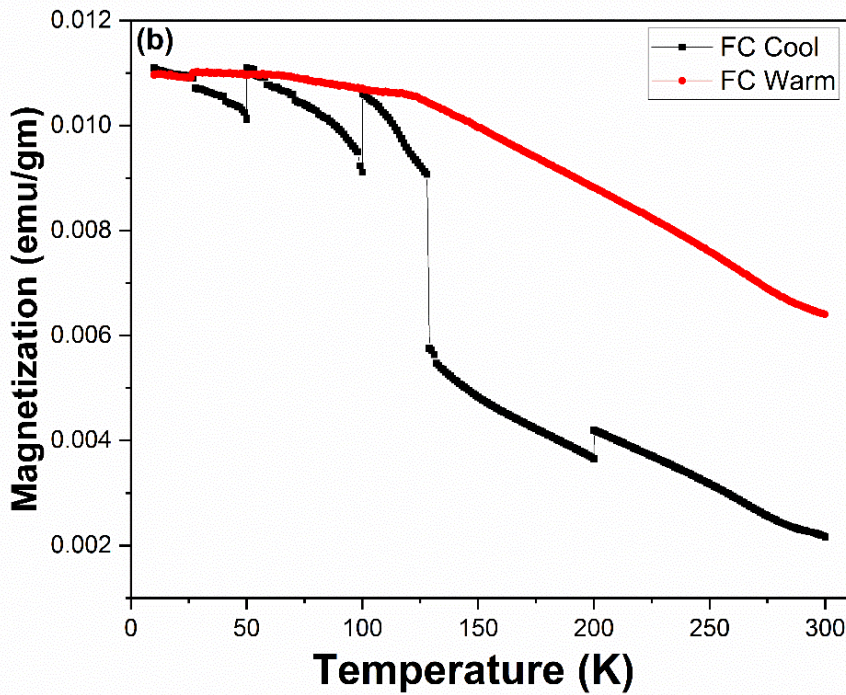


Figure 4.10(b): FC Magnetic memory measurement of $x = 0.05$ sample at 100 Oe.

A decrease in the step-like FC magnetization curve with decreasing temperature of $x = 0$ sample points towards the presence of randomly frozen spin

states at lower values of temperature. $x = 0.05$ sample, on the other hand, can only retrieve its memory at temperatures 25, 50 and 100 K. There also seems to be an anomaly in the nature of FC curve which is different from that observed in Fig. 4.8(c). Thus, $x = 0.05$ sample is unable to retrieve its past thermal history in a quintessential manner as no distinctive step-like behaviour can be observed at the stopping temperatures of 125 K and 200 K while heating the sample.

References

1. C. Wang, Y. D. Li, G. H. Zhang, J. Zhuang and G. Q. Shen, "Synthesis of SnSe in various alkaline media under mild conditions," *Inorg. Chem*, vol. 39, 4237 (2000).
2. H. Xu, et al., "Flexible SnSe photodetectors with ultrabroad spectral response up to 10.6 μm enabled by photobolometric effect," *ACS Appl. Mater. Interfaces*, vol. 12, 35250 (2020).
3. M. Kang, et al., "Photodetector based on multilayer SnSe₂ field effect transistor," *J. Nanosci. Nanotechnol.*, vol. 18, 4243 (2017).
4. K. Chung, D. Wamwangi, M. Woda, M. Wuttig and W. Bensch, "Investigation of SnSe, SnSe₂ and Sn₂Se₃ alloys for phase change memory applications," *J. Appl. Phys.*, vol. 103, 083523 (2008).
5. W. Shi, M. Gao, J. Wei, J. Gao, C. Fan, E. Ashalley, H. Li and Z. Wang, "Tin Selenide (SnSe): Growth, Properties, and Applications," *Adv. Sci.*, vol. 5, 1700602 (2018).
6. I. Lefebvre, M. A. Szymanski, J. Oliver-Fourcade and J. C. Jumas, "Electronic structure of tin monochalcogenides from SnO to SnTe," *Phs. Rev. B*, vol. 58, 1896 (1998).
7. X-L. Shi, X. Tao, J. Zou and Z-G. Chen, "High-performance thermoelectric SnSe: Aqueous synthesis, innovations, and challenges," *Adv. Sci.*, vol. 7, 1902923 (2020).
8. S-K. Cha, S. Im, B. Ryu and Y-S. Kim, "Facile phase transition to β - from α -SnSe by uniaxial strain," *Curr. Appl. Phys.*, vol. 45, 45 (2023).
9. A. M. Elkorashy, "Optical constants of tin selenide single crystals by interference method," *J. Phs. Chem. Solids*, vol. 51, 289 (1990).
10. M. Gharibshahi, F. Jamali-Sheini and R. Yousefi, "Effect of ultrasonic irradiation time on the physical and optoelectronic properties of SnSe nanorods," *Surf. Interfaces*, vol. 27, 101433 (2021).

11. A. T. Duong et al., "Achieving $zT = 2.2$ with Bi-doped n-type SnSe single crystals," *Nat. Commun.*, vol. 7, 13713 (2016).
12. C. Zhou et al., "Polycrystalline SnSe with a thermoelectric figure of merit greater than the single crystal," *Nat. Mater.*, vol. 20, 1378 (2021).
13. S. Patel, S. H. Chaki and P. C. Vinodkumar, "Pure SnSe, In and Sb doped SnSe single crystals-Growth, structural, surface morphology and optical bandgap study," *J. Cryst. Growth*, vol. 522, 16 (2019).
14. C. H. Hu, M. H. Chiang, M. S. Hsieh, W. T. Lin, Y. S. Fu and T. F. Guo, "Phase formation morphology evolution and tunable bandgap of $\text{Sn}_{1-x}\text{Sb}_x\text{Se}$ nanocrystals," *Cryst. Eng. Comm.*, vol. 16, 1786 (2014).
15. N. Xin, Y. Li, G. Tang and L. Shen, "Enhancing thermoelectric performance of K-doped polycrystalline SnSe through band engineering tuning and hydrogen reduction," *J. Alloy. Comp.*, vol. 899, 163358 (2022).
16. G. Han et al., "Chlorine-enabled electron doping in solution-synthesized SnSe thermoelectric nanomaterials," *Adv. Energy Mater.*, vol. 7, 1602328 (2017).
17. F. Jamali-Sheini, M. Cheraghizade and R. Yousefi, "Electrochemically synthesis and optoelectronic properties of Pb- and Zn- doped nanostructured SnSe films," *App. Surf. Sci.*, vol. 443, 34.5 (2018).
18. K. Ananthi, K. Thilakavathy, N. Muthukumarasamy, S. Dhanapandian, K. R. Murali, "Properties of pulse plated SnSe films," *J. Mater. Sci. Mater. Electron.*, vol. 23, 1338 (2012).
19. D. Shikha, V. Mehta, J. Sharma, R. P. Chauhan, "Effect of deposition temperature on structural, optical and electrical properties of nanocrystalline SnSe thin films," *J. Mater. Sci. Mater. Electron.*, vol. 28, 2487 (2017).
20. T. Pei et al., "Epitaxy of Ultrathin SnSe Single Crystals on Polydimethylsiloxane: In-Plane Electrical Anisotropy and Gate-Tunable Thermopower," *Adv. Electron. Mater.*, vol. 2, 1600292 (2016).

21. M. R. Pallavolu, S. K. Vishwanath and S. W. Joo, "Development of indium (In) doped SnSe thin films for photovoltaic applications," *Mater. Lett.*, vol. 281, 128714 (2020).
22. S. Wang et al., "Low temperature thermoelectric properties of p-type doped single-crystalline SnSe," *App. Phys. Lett.*, vol. 112, 142102 (2018).
23. L-D. Zhao et al., "Ultralow thermal conductivity and high thermoelectric figure of merit in SnSe crystals," *Nature*, vol. 508, 373 (2014).
24. M. Luo, Y. Xu and Y. Shen, "Magnetic properties of SnSe monolayer doped by transition-metal atoms: A first-principle calculation," *Results Phys.* vol. 17, 103126 (2020).
25. S. Isber and X. Gratens, "Crystal growth and magnetic properties of tin selenide-doped europium $\text{Sn}_{1-x}\text{Eu}_x\text{Se}$," *J. Magn. Magn Mater.*, vol. 322, 1113 (2010).
26. J. Lu, L. Guo, G. Xiang, Y Nie and X. Zhang, "Electronic and magnetic tunability of SnSe monolayer via doping of transition-metal atoms," *J. Electron. Mater.*, vol. 49, 290 (2020).
27. R. Du et al., "Two-dimensional multiferroic material of metallic p-doped SnSe," *Nat. Commun.*, vol. 13, 6130 (2022).
28. K. Ohta, *Physics and Chemistry of Molecular Assemblies*, World Scientific, 2020, pp. 1-40.
29. D. Balzar and H. Ledbetter, "Voigt-function modeling in Fourier analysis of size- and strain-broadened X-ray diffraction peaks," *J. Appl. Crystallogr.*, vol. 26, 97 (1993).
30. A. K. Zak, W. H. A. Majid, M. E. Abrishami and R. Yousefi, "X-ray analysis of ZnO nanoparticles by Williamson-Hall and size-strain plot methods," *Solid State Sci.*, vol. 13, 251(2011).
31. C. Murugesan and G. Chandrasekaran, "Impact of Gd^{3+} -substitution on the structural, magnetic and electrical properties of cobalt ferrite nanoparticles," *RSC Adv.*, vol. 5, 73714 (2015).

32. X. Xu, "In-plane anisotropies of polarized Raman response and electrical conductivity in layered tin selenide," *ACS Appl. Mater. Interfaces*, vol. 9, 12601 (2017).
33. S. Zhao et al., "Controlled synthesis of single-crystal SnSe nanoplates," *Nano Res.* vol. 8, 288 (2015).
34. T. Sriv et al., "Optical phonons of $\text{SnSe}_{(1-x)}\text{Se}_x$ layered semiconductor alloys," *Sci. Rep.*, vol. 10, 11761 (2020).
35. I. Pethes et al., "Atomic level structure of Ge-Sb-S glasses: Chemical short range order and long Sb-S bonds," *J. Alloy. Comp.*, vol. 774, 1009 (2019).
36. G. Spaggiari et al., "Exploring Cu-doping for performance improvement in Sb_2Se_3 photovoltaic solar cells," *Int. J. Mol. Sci.*, vol. 23, 15529 (2022).
37. N. E. Makori, I. A. Amatalo, P. M. Karimi and W. K. Njoroge, "Optical and electrical properties of SnSe thin films for solar cell applications," *Am. J. Consens. Mater. Phys.*, vol. 4, 87 (2014).
38. P. A. Sharma, S. B. Kim, T. Y. Koo, S. Guha and S-W. Cheong, "Reentrant charge ordering transition in the manganites as experimental evidence for a strain glass," *Phys. Rev. B*, vol. 71, 224416 (2005).
39. B. Sarkar, B. Dalal, V. D. Ashok, K. Chakrabarti, A. Mitra and S. K. De, "Magnetic properties of mixed spinel $\text{BaTiO}_3\text{-NiFe}_2\text{O}_4$ composites," *J. Appl. Phys.*, vol. 115, 123908 (2014).
40. C. R. Shankar and P. A. Joy, "Magnetic properties of the self-doped lanthanum manganites $\text{La}_{1-x}\text{MnO}_3$," *Phys. Rev. B*, vol. 72, 024405 (2005).
41. Y. Sun, M. B. Salamon, K. Garnier and R. S. Averback, "Memory Effects in an Interacting Magnetic Nanoparticle System," *Phys. Rev. Lett.*, vol. 91, 167206 (2003).